Fluid reservoir in the Hyuga-nada accretionary prism near the Kyushu-Palau ridge: insights from a passive seismic array

[1]Takeshi Akuhara
[2]Yusuke Yamashita
[3]Shukei Ohyanagi
[3]Yasunori Sawaki
[1]Tomoaki Yamada
[1]Masanao Shinohara

[1]Earthquake Research Institute, The University of Tokyo, Tokyo, Japan
[2]Disaster Prevention Research Institute, Kyoto University, Kyoto, Japan
[3]Graduate School of Science, Kyoto University, Kyoto, Japan

Corresponding author:
Takeshi Akuhara (akuhara@eri.u-tokyo.ac.jp)

Key points

- The shear wave velocity structures of the shallow Hyuga-nada accretionary prism were derived using a passive seismic array.
- A low shear velocity zone exists ~3–4 km below the seafloor, possibly indicative of a fluid reservoir.
- A Fault induced by the subducting Kyushu–Palau Ridge may act as a fluid pathway, supplying fluids to the reservoir.

Abstract

Shear wave velocity (Vs) estimations of accretionary prisms can pose unique constraints to the physical properties of rocks, which are hard to obtain from compressional velocities (Vp) alone. Thus, it would help better understand the fluid processes of the accretion system. This study investigates the Vs structure of the Hyuga-nada accretionary prism using an array of ocean-bottom seismometers (OBSs) with a 2 km radius. Teleseismic Green's functions and a surface wave dispersion curve are inverted to one-dimensional Vs structures using transdimensional inversion. The results indicate the presence of a low-velocity zone 3–4 km below the seafloor. The reduced Vs is consistent with a reduced Vp feature obtained in a previous seismic refraction survey. From its high Vp/Vs ratio, we conclude that the low velocities represent high pore fluid pressure. In addition, the resolved lithological boundary exhibits a sharp offset that extends laterally across the OBS array. We attribute this offset to a blind fault below while acknowledging other possibilities, such as due to mud diapirism. The predicted fault is located at the Kyushu–Palau Ridge flank, oriented roughly parallel to the ridge axis, and thus likely caused by ridge subduction. The fracture caused by the ridge subduction may act as a fluid conduit, forming a fluid reservoir beneath the well-compacted sediment layers.

Plain language summary

Propagation speeds of seismic S-waves offer unique constraints on physical properties in shallow subduction zones, which is hard to know from only seismic P-wave velocity. This study investigates the subsurface structure in Hyuga-nada in the southwestern Japan subduction zone by exploring S-wave speeds. For this purpose, we use natural seismic and noise data recorded by densely installed ocean-bottom seismometers. The results reveal a region with a reduced S-wave velocity at a depth of ~3–4 km below the seafloor, which may be a water reservoir. The depth of the potential water reservoir changes abruptly across the array. This offset may suggest the presence of a hidden fault

below, although we cannot exclude other possibilities. We propose that a fault created by subducting seamounts acts as a conduit that transports water to the reservoir.

Keywords

Hyuga-nada

Kyushu–Palau Ridge

Fluid reservoir

Transdimensional inversion

Ocean-bottom seismometer

1. Introduction

Fluids, which may influence the slip behaviors of faults by increasing pore pressure, are crucial for understanding the subduction–accretion system. They have been associated with the seismic cycle (Van Dinther et al., 2013), the genesis of slow earthquakes (Saffer & Wallace, 2015), and wedge development (Wang & Hu, 2006). Recent studies have shown that subducted reliefs such as seamounts and ridges play a critical role in hydrology. Seamounts reportedly induce fractures within the overriding plate, which increases permeability (Chesley et al., 2021; Sahling et al., 2008; Sun et al., 2020). High-resolution P-wave velocity (Vp) structures provided by active-source seismic surveys have illuminated fluid distribution in accretionary prisms. Still, additional constraints from S-wave velocity (Vs) are essential to gain further insights into subsurface rock properties, especially the pore fluid pressure (Akuhara et al., 2020; Arnulf et al., 2021; Tsuji et al., 2011).

Hyuga-nada, located in the westernmost southwestern Japan subduction zone, is a region facing ridge subduction (**Figure 1**). The incoming Philippine Sea Plate hosts the Kyushu–Palau Ridge (KPR) with a NNW–SSE strike. The subducted portion of this ridge has been identified by seismological studies employing either passive or active seismic sources (Park et al., 2009; Yamamoto et al., 2013). The subduction of the KPR beneath the Kyushu started at 5 Ma; the convergence direction was almost parallel to the ridge axis and perpendicular to the trench (Mahony et al., 2011). At 1–2 Ma, the subduction direction slightly rotated counterclockwise; consequently, the subduction accompanies the right-lateral motion (Itoh et al., 1998; Yamazaki & Okamura, 1989). Tectonic tremors and very-low-frequency earthquakes, both are members of slow earthquakes, intermittently occur near the KPR with an interval of 1–3 years (Baba et al., 2020; Tonegawa et al., 2020; Yamashita et al., 2015, 2021). As suggested for other regions worldwide, these slow earthquake activities may reflect a fluid-rich environment near the plate interface (Saffer & Wallace, 2015). However, little is known about the fluid processes (e.g., fluid sources, pathways, reservoirs) in this region.

High-resolution structures of the accretionary prism in this region were obtained in previous active-source seismic surveys (Nakanishi et al., 2018; Nishizawa et al., 2009; Park et al., 2009). **Figure 1**c shows a P-wave velocity (Vp) model based on a refraction survey (Nakanishi et al., 2018). Overall, the accretionary prism shows Vp of 2–4 km/s, and the subducting Philippine Sea Plate has a higher velocity of >6 km/s beneath the prism. Interestingly, velocity inversion with depth is noticeable at ~2 km beneath the seafloor (**Figure 1**d). Nishizawa et al. (2009) reported a similar low-velocity zone (LVZ) beneath another independent seismic profile in Hyuga-nada. These LVZs may indicate fluid-rich conditions, although previous studies have not provided a detailed interpretation. The challenges are the modest sensitivity of the refraction surveys to thin LVZs with a sharp velocity contrast and the interpretation of physical properties based on Vp alone.

This study investigates the shear wave velocity (Vs) structure by utilizing a dense passive seismic array of ocean-bottom seismometers (OBSs) deployed in the Hyuga-nada region. Traditionally, active-source seismic surveys play a central role in constraining Vs structures within shallow marine sediments (e.g., Tsuji et al., 2011). However, in contrast to Vp, investigating Vs via active seismic sources is challenging because of the inefficient excitation of shear waves beneath the seafloor. In recent years, various elements of passive seismic records have been increasingly used to overcome this problem, including ambient surface wave noise (Mosher et al., 2021; Tonegawa et al., 2017; Yamaya et al., 2021; Zhang et al., 2020), teleseismic body waves (Agius et al., 2018; Akuhara et al., 2020), and a combination of them (Doran & Laske, 2019). This study attempts to solve Vs structures through the transdimensional inversion of teleseismic body waves and a surface wave dispersion curve (DC). Based on the results, we discuss the hydrological features in Hyuga-nada, which can be linked to the subducted KPR..

2. Passive seismic array

This study uses a passive seismic array of 10 OBSs installed in the Hyuga-nada region. The OBSs continuously recorded seismic waveforms from March 30, 2018, to September 30, 2018 (Figure 1). Five OBSs (HDA01–05) were evenly installed within a radius of 1 km, whereas the other five OBSs (HDA06–10) were placed within 2 km, around the same center. Each OBS contains short-period three-component sensors

(LE-3Dlite, Lennartz Electronic GmbH, Germany) and a gimbal to maintain the sensor's horizontality. The seismometer positions were constrained by acoustic positioning from a research vessel. The sensor orientations were determined from the particle motion of teleseismic Rayleigh waves (Sawaki et al., 2022; Stachnik et al., 2012; see text S1, Figure S1, and Table S1 in the supporting information).

The array aimed to explore the potential of passive source methods for imaging shallow sediment structures. Another broadband OBS was deployed at the center of the array circle, but we failed to recover it. The array was placed on the refraction seismic survey line such that the tomography model could be used as a reference (Nakanishi et al., 2018; Figure 1). According to this refraction survey, the interface of the Philippine Sea Plate subducts to ~10–11 km depth beneath the array. The seafloor topography is relatively gentle, with a slight slope to the northeast, resulting in a height difference of only ~120 m over the 4 km diameter (**Figure 1**b). Therefore, its effects on surface and body wave propagation are negligible.

3. Method

This section elaborates on procedures we adopted to estimate Vs structures beneath the OBSs. The DC measurements from ambient noise records are described in Section 3.1. In Section 3.2, we describe the procedure we used to retrieve the Green's function (GF) from teleseismic P-waves. Subsequently, the acquired DC and GFs were inverted to one-dimensional (1D) Vs structures using a transdimensional, stochastic inversion scheme, as discussed in Section 3.3.

3.1 Rayleigh wave dispersion curve

We retrieved Rayleigh waves propagating across the array from half-year-long records of ambient seismic noise. For this purpose, we employ a series of signal processing steps: cutting records into one-hour-long segments, detrending time series, downsampling data from 200 to 10 samples per second, deconvolution with instrumental responses, spectral whitening, and one-bit normalization in the time domain (Bensen et al., 2007). Cross-correlation functions (CCFs) of vertical components are then calculated between each station pair and stacked over the entire observation period. Figure 2 shows vertical-component CCFs obtained from all station pairs. The fundamental Rayleigh mode dominates CCFs at 0.2–0.4 Hz with an apparent velocity of ~0.5 km/s.

Based on the assumption of a laterally homogeneous structure beneath the array, the aggregation of CCFs in Figure 2 can be considered a virtual short gather recorded by a linear array. We estimate an averaged DC across the OBS array by applying the frequency–wavenumber (FK) analysis to this virtual shot gather. This treatment can significantly extend the high-frequency (or short-wavelength) limit of phase velocity measurements without suffering from spatial aliasing effects (Gouédard et al., 2008). This feature benefits this study because acquiring higher-frequency phase velocities is essential to constrain shallow structures of marine sediments.

The FK domain spectrum obtained from these virtual records shows the DC of the fundamental Rayleigh wave, which is traceable from 0.15 Hz (near the resolution limit) to 0.5 Hz (**Figure 3**). The DC shows minor deflection at ~0.4 Hz, which we consider an artifact from the specific array configuration. In the higher frequency range between 0.5–1.0 Hz, the spectrum exhibits a complex pattern, and it is hard to distinguish the actual signal from artificial sidelobes. A relatively continuous feature can be observed at a frequency of >1 Hz, corresponding to the higher-mode Rayleigh wave, but the mode identification is nontrivial because of the ambiguity in the range of 0.5–1.0 Hz.

3.2 Teleseismic Green's functions

We extract P waveforms of teleseismic events with M>5.5 and an epicentral distance of 30–90°. Each extracted record is decimated to 20 samples per second, and two horizontal components were rotated to radial and transverse directions. We only retain data with a signal-to-noise ratio (SNR) above 3.0 on the vertical component. In this study, the SNR is defined as the root-mean-square amplitude ratio of 30 s time windows before and after P arrival. The GFs of teleseismic P-waves are retrieved from these time windows with the blind deconvolution technique (Akuhara et al., 2019). In contrast to conventional receiver function methods that only solve radial-component GFs, both radial- and vertical-component GFs can be estimated with this method. The retrieval of vertical-component GFs is crucial for ocean-bottom settings because intense water multiples dominate the vertical-component records. We use 60 s time windows for the deconvolution and apply a Gaussian low-pass filter to the results. The Gaussian parameter (i.e., standard deviation) is set to 8, corresponding to a 10% gain at ~4 Hz.

The radial-component GFs are mostly coherent across the array, especially for the first 4 seconds (Figure 4a; see also Figure S2–S11 for wiggle plots against event back azimuths). A negative peak is predominant at ~2.0–2.5 s after the direct P arrival. This coherency quantitatively justifies the 1D structure assumption we made for the FK analysis. At zero lag time, a peak corresponding to the direct P arrival is not evident, indicating the nearly vertical incidence of the P phase due to the low Vp of unconsolidated sediments. The vertical-component GFs show reverberations within the seawater column (Figure 4b). The first reverberation with a positive polarity is evident at 3.1 s, and the second one can be observed at 6.2 s and has a reversed polarity.

Although we did not use these vertical-component GFs for the inversion analysis, the good recovery of water reverberations to some degree validates the radial component estimations.

3.3 Transdimensional Bayesian inversion

We use a transdimensional Bayesian interface and the reversible-jump Markov chain Monte Carlo (RJMCMC) algorithm (Green, 1995) for the inversion of the dispersion and GF data to an isotropic 1D Vs model beneath each OBS. The RJMCMC performs probabilistic sampling of model parameters, allowing the dimension of the model parameter space to be unknown. In our case, the algorithm automatically selects the number of layers in the 1D subsurface structure model. The transdimensional Bayesian inversion aims to estimate the posterior probability of the model parameter, $\boldsymbol{m}_k$, with the given data, $\boldsymbol{d}$, that is, $P(k, \boldsymbol{m}_k|\boldsymbol{d})$, where k is a parameter determining the model-space dimension. Based on the Bayes' theorem, the posterior probability is proportional to the product of the prior probability, $P(k, \boldsymbol{m}_k)$, and the likelihood, $P(\boldsymbol{d}|k, \boldsymbol{m}_k)$:

$$P(k, \boldsymbol{m}_k|\boldsymbol{d}) \propto P(k, \boldsymbol{m}_k)P(\boldsymbol{d}|k, \boldsymbol{m}_k).$$

3.3.1 Model parameters

We assume that the subsurface structure consists of k layers. Each layer has constant seismic P- and S-wave velocities and density; the structure's lateral heterogeneity, anisotropy, and dissipation are ignored. We defined a model vector $\boldsymbol{m}_k = (z_1, \cdots, z_{k-1}, \delta\beta_1, \cdots, \delta\beta_{k-1}, \sigma_{DC}, \sigma_{GF})^T$, where $\delta\beta_i$ is the S-wave velocity perturbation relative to a reference model and z_i is the bottom depth of the ith layer. The other two parameters, σ_{DC} and σ_{GF}, represent the standard deviations of data noise, which are also solved within the hierarchical Bayesian model (Bodin et al., 2012). Based on a given set of model parameters, first, a Vs value of each layer is extracted from the reference model. The perturbation $\delta\beta_i$ is then added to the extracted value. Similarly, Vp is obtained from the reference model, but without perturbation. The density is calculated from the Vp using an empirical relationship (Brocher, 2005). We fix the properties of the bottom half-space (i.e., kth layer) to stabilize the forward calculation of dispersion curves: Vs is set to 4.0 km/s and Vp and the density are scaled to Vs using the empirical law of Brocher (2005). For the seawater layer, we assume an acoustic velocity of 1.5 km/s and thickness of 2.388 km, which is the average station depth. The reference model was constructed from the two-dimensional (2D) P-wave velocity model of Nakanishi et al. (2008), as shown in Figure 1c, with the empirical scaling law that converts Vp into Vs (Brocher, 2005). Since the lateral velocity variation is small across the array, we construct a single reference model and apply it to all stations.

3.3.2 Likelihood

We calculate the likelihood $P(\boldsymbol{d}|k,\boldsymbol{m}_k)$ based on the assumption of Gaussian noise distribution:

$$P(\boldsymbol{d}|k,\boldsymbol{m}_k) = P(\boldsymbol{d}_{DC}|k,\boldsymbol{m}_k)P(\boldsymbol{d}_{GF}|k,\boldsymbol{m}_k),$$

$$P(\boldsymbol{d}_{DC}|k,\boldsymbol{m}_k) = \frac{1}{\sqrt{(2\pi)^{N_{DC}}|\mathbf{C}_{DC}|}}\exp\left\{-\frac{1}{2}[\boldsymbol{g}_{DC}(k,\boldsymbol{m}_k)-\boldsymbol{d}_{DC}]^{\mathrm{T}}\mathbf{C}_{DC}^{-1}[\boldsymbol{g}_{DC}(k,\boldsymbol{m}_k)-\boldsymbol{d}_{DC}]\right\},\#$$

and

$$P(\boldsymbol{d}_{GF}|k,\boldsymbol{m}_k) = \frac{1}{\sqrt{(2\pi)^{N_{GF}}|\mathbf{C}_{GF}|}}\exp\left\{-\frac{1}{2}[\boldsymbol{g}_{GF}(k,\boldsymbol{m}_k)-\boldsymbol{d}_{GF}]^{\mathrm{T}}\mathbf{C}_{GF}^{-1}[\boldsymbol{g}_{GF}(k,\boldsymbol{m}_k)-\boldsymbol{d}_{GF}]\right\},\#$$

where $\mathbf{C}_{\mathrm{DC}}$ and $\mathbf{C}_{\mathrm{GF}}$ are the covariance matrices of the DC and GF data noise, respectively, and $\boldsymbol{g}_{DC}$ and $\boldsymbol{g}_{GF}$ are the synthetic DC and GF, respectively. The data vector, $\boldsymbol{d}$, consists of DC and GF data vectors, denoted as $\boldsymbol{d}_{DC}$ and $\boldsymbol{d}_{GF}$, respectively, with a length of N_{DC} and N_{GF}, respectively. We assume the temporal correlation of noise for GFs, which originates from the Gaussian low-pass filter, and a constant noise level across the entire time series. The corresponding covariance matrix can be expressed by $\mathrm{C}_{\mathrm{GF}ij} = \sigma_{GF}^2 r^{(j-i)^2}$, where r is pre-determined from the Gaussian filter width (Bodin et al., 2012) and σ_{GF} is a standard deviation of the data noise. We ignore off-diagonal components of the DC covariance matrix and assumed frequency-independent measurement error, which results in $\mathrm{C}_{\mathrm{DC}ij} = \sigma_{DC}^2\delta_{ij}$, where σ_{DC} is a standard deviation of DC data noise and δ_{ij} is the Kronecker delta. The standard deviations (i.e., σ_{DC} and σ_{GF}) are treated as hyper parameters and solved together with the model parameters (Bodin et al., 2012).

3.3.3. Prior probabilities

We assume truncated uniform distributions for the prior probability of k, σ_{DC}, and σ_{GF}. We also assume the following limits: $[k_{min}, k_{max}) = [1, 51)$ for k, $[\sigma_{DCmin}, \sigma_{DCmax}] = [0.005, 0.090]$ for σ_{DC} (unit in km/s), and $[\sigma_{GFmin}, \sigma_{GFmax}] = [0.02, 0.07]$ for σ_{GF}. We tested several choices for these parameters to find that the resulting velocity structures did not change significantly. We set the minimum limit of the layer depths to z_{min} =2.388 (water depth) and the maximum to z_{max} =15 km and use the Dirichlet partition prior with unit concentration parameters (Dosso et al., 2014). This setting corresponds to a non-informative prior: the prior probability remains constant no matter where the layer boundary is between z_{min} and z_{max}. We use the Gaussian distribution with a zero mean for the Vs anomalies. The Gaussian width (i.e., standard deviation $\sigma_{\delta\beta}$) must reflect how reliable the reference model is. We set this parameter to 0.2 km/s. In summary, the joint prior can be expressed as follows:

$$P(k, \boldsymbol{m}_k) = \frac{1}{k_{max} - k_{min}} \cdot \frac{1}{\sigma_{DCmax} - \sigma_{DCmin}} \cdot \frac{1}{\sigma_{GFmax} - \sigma_{GFmin}} \cdot \frac{k!}{(z_{max} - z_{min})^k} \cdot \prod_{i=1}^{k-1} \frac{1}{\sigma_{\delta\beta}\sqrt{2\pi}} \exp\left(-\frac{\delta\beta_i^2}{2\sigma_{\delta\beta}^2}\right).$$

We confirmed that our inversion code implements the prior probability as intended by performing MCMC, forcing the likelihood to be zero (Figure S12).

3.3.4. Probabilistic sampling with parallel tempering

The RJMCMC algorithm aims to sample the posterior probability $P(k, \boldsymbol{m}_k|\boldsymbol{d})$ through iteration. At each iteration, a new model $(k', \boldsymbol{m}'_{k'})$ is proposed by either (1) adding a layer, (2) removing a layer, (3) moving a layer interface, (4) perturbing the S-wave velocity of a layer, or (5) perturbing the standard deviation of the data noise. One of the above-mentioned five procedures is randomly selected at each iteration to generate a new model. The proposed model is accepted at a probability α_{MHG}, which is defined as the tempered Metropolis–Hastings–Green criterion (Green, 1995):

$$\alpha_{MHG} = \min\left\{1, \frac{P(k', \boldsymbol{m}'_{k'})}{P(k, \boldsymbol{m}_k)} \left[\frac{P(\boldsymbol{d}|k', \boldsymbol{m}'_{k'})}{P(\boldsymbol{d}|k, \boldsymbol{m}_k)}\right]^{\frac{1}{T}} \frac{Q(k, \boldsymbol{m}_k|k', \boldsymbol{m}'_{k'})}{Q(k', \boldsymbol{m}'_{k'}|k, \boldsymbol{m}_k)} |\boldsymbol{J}|\right\}, \#$$

where $P(k, \boldsymbol{m}_k)$ is the prior probability; $Q(k', \boldsymbol{m}'_{k'}|k, \boldsymbol{m}_k)$ is the probability that a transition from $(k, \boldsymbol{m}_k)$ to $(k', \boldsymbol{m}'_{k'})$ is proposed, and $|\boldsymbol{J}|$ is the Jacobian compensating for a unit volume change in the model space. The exponent T (> 1), which represents a temperature that loses the acceptance criterion, is a modification of the original Metropolis–Hastings–Green criterion. In the parallel tempering method (Geyer & Thompson, 1995; Sambridge, 2014), differently tempered Markov chains are run in parallel. At the end of each iteration, 10 pairs of chains are probabilistically allowed to swap the temperatures. Based on this swap, the random walk can undergo a long jump in the model space and efficiently converge to the global maximum.

The inversion involves 1,000,000 iterations, including the first 800,000 iterations of the burn-in period. In total, 100 Markov chains are run in parallel, 20 of which have a unit temperature and are used to evaluate posterior probabilities. We only save the models every 2,000 iterations to avoid artificial correlation between samples.

4. Results

The ensemble of model parameters sampled by the transdimensional inversion provides insights into the probable range of a 1D Vs structure beneath each station. Figure 5 shows the inversion results obtained at HDA06. The posterior marginal probability of V_S as a function of depth indicates a well-converged solution with a clearly defined peak at each depth. Other diagnostic information, such as the evolution of log-likelihood and acceptance ratio of proposals, is shown in Figure S13 and Table S2, respectively. According to the mode value at each 0.3 km depth (green line, Figure 5), the velocity increases up to a depth of 4.8 km, with sharp, positive velocity contrasts at depths of 2.7 and 3.9 km. Although less clear, these discontinuities can be seen in the maximum a posteriori (MAP) estimate (purple line, Figure 5). We conclude that these contrasts reflect different lithologies of sediments and refer to the layers as sedimentary units 1–3 (U1–3), from top to bottom.

Beneath this unit sequence, Vs abruptly drops to form a LVZ. The top of the LVZ is 0.1 km deeper than the depth at which the referenced Vp tomography model exhibits velocity inversion. Note that our prior Vs information already incorporates the velocity inversion that can be observed in the Vp model (black curve, Figure 5f). The inversion analysis requires the further reduction of Vs, suggesting a high Vp/Vs ratio in the LVZ: based on the assumption of a Vp of 3.4 km/s from the Vp tomography model, the Vp/Vs ratio corresponds to 2.8. However, this estimation likely overestimates Vp/Vs ratio. This is because the reference Vp tomography model has a coarser vertical resolution than Vs profiles obtained in this study, subject to smoothing constraints. Thus, we smoothed the Vs profile using a running window of 1.5 km depth to mimic the vertical resolution of seismic tomography (Figure S14). The window length of 1.5 km was chosen by trial and error so that Vs profile exhibits a similar degree of smoothness to the reference Vp model. Even after this smoothing, the Vp/Vs profile culminates at the LVZ with a maximum value of 2.5.

Inversion results from other stations show similar first-order features. Three layers (i.e., U1–3) are discernible immediately beneath the seafloor, and a LVZ can be detected beneath them, especially evident with mode estimations (Figure 6). An exception is HDA01 without a LVZ. This absence of LVZ beneath HAD01 could be artificial, considering that Vs profiles from the other stations consistently exhibit a LVZ. Since the LVZ is the center of interest, we exclude HDA01 results from the discussion for simplicity. Following the last paragraph, we calculate smoothed Vp/Vs profiles of each station. The resulting Vp/Vs profile shows a peak at the LVZ depth for most stations (Figure 7). The peak values from mode estimations are consistent among HDA02, 03, 04, 05, 06, 08, and 09, ranging from 2.5–2.7. Stations HDA07 and HDA10 show relatively lower Vp/Vs, 2.2 and 2.0, respectively, but the probability distribution of those stations has an elongated tail toward higher Vp/Vs. Thus, the Vp/Vs ratio of 2.5–2.7 may also be applicable to these two stations.

To quantify the depth of each lithological boundary, we searched for the depth of maximum velocity contrast within a given depth range. This search was performed for all 1D S-wave velocity structures sampled in the inversion. The aggregation of all results provides statistics for the lithological boundary depths. We set depth ranges for this search to 2.3–3.1 km for the boundary U1–U2, 3.1–5.5 km for U2–U3, 4.0–7.0 km for U3–LVZ, and 5.5–9.5 km for the bottom of the LVZ. The resulting median estimates are shown as background colors in Figures 6 and 7. In addition, 68% confidence intervals are shown in Figure 8b. Note that this error estimation tends to be biased toward magnifying uncertainties because the transdimensional inversion can produce ineffective (i.e., too thin) layers at random depths with a considerable velocity contrast. Hence, we chose to display the 68% confidence intervals in Figure 8b rather than the commonly used 95% intervals.

The above qualitative estimates of uncertainties confirmed the lateral variation in the depth of the top of the LVZ: the lithological boundary deepens on the southwestern side, whereas it becomes shallower on the northeastern side (Figure 8a). The depth offset is sharp: ~1 km vertical offset within a distance of 0.5 km. The green vertical bars in Figure 8c show a 68% range of theoretical arrivals of the Ps converted phase from the top of the LVZ, which is drawn from MCMC samples. For all stations except HDA03, these timings predict a negative phase arrival well. The negative phase arrives at the northeastern stations (HDA06, 02, 08, and 07) ~0.5 s earlier than at the southwestern stations (HDA10, 09, 04, and 05). This offset in the time domain must be responsible for the offset in the depth domain. For HDA03, the theoretical arrival does not match negative phase arrivals. Multiple reflections from the shallower layers may overprint a Ps phase from the top of the LVZ.

The present study fixes a P-wave velocity structure at a single reference model and applies it to all stations, ignoring the presence of lateral heterogeneities and uncertainties in the reference model. However, such a fixed Vp could minorly bias Vs estimation because P-wave GFs (or receiver functions) have secondary sensitivity to Vp/Vs ratios (e.g., Zhu, L., Kanamori, 2000). To quantify this effect, we solved Vp anomalies as well as Vs, where a Gaussian distribution with a standard deviation of 0.15 km/s is used as the prior probability for Vp anomaly. The results show that the main feature (i.e., the LVZ) does not change, irrespective of whether Vp is solved (Figure S15). The posterior probability of Vp remains nearly identical to the prior probability below a depth of 4 km, suggesting that the dataset is only sensitive to the shallow part of the Vp structure. The longer time window of GFs could constrain Vp/Vs ratios of the LVZ, but unfortunately, GFs do not show good consistency for phases arriving later than 4 s (see Figure 4a).

Another concern is overfitting. The transdimensional inversion could unnecessarily add many thin layers to cause overinterpretation of input data. In theory, this issue can be avoided by the adopted transdimensional inversion scheme but could occur with an inappropriate parameterization made for the likelihood, for example. To see whether the obtained LVZ is robust, we enforced a smaller number of layers by setting k_{max} to 21. Still, we observe an evident LVZ (Figure S16). As another test case, we conducted a fixed-dimensional inversion by fixing k at 20. The other parameters, including layer depths, are allowed to vary freely. We found that this fixed-dimensional setting fails to reach a well-converged solution, highlighting the efficient model search by the transdimensional algorithm (Figure S17). This kind of advantage in the transdimensional scheme has not been discussed elsewhere, to the best knowledge, but should be investigated more in the future.

5. Geological interpretation

The inversion results present a remarkable low-velocity, high Vp/Vs feature with a velocity inversion. Typically, marine sediments undergo a monotonic increase in Vs with increasing depth because of compaction (Hamilton, 1979). The velocity inversion observed in this study is unexpected. A plausible cause for the observed velocity inversion is high pore fluid pressure. Based on theory and experiments, it is known that high pore fluid pressure increases the Vp/Vs ratio of marine sediments (Dvorkin et al., 1999; Prasad, 2002), which agrees with our results. Therefore, we interpret that the LVZ represents a fluid reservoir. Aligned cracks could also explain the high Vp/Vs ratio even in the absence of fluid through anisotropic effects (X. Q. Wang et al., 2012). However, we find that numerical modeling based on a scattering theory with penny-shaped parallel cracks (Hudson, 1981) fails to explain such high Vp/Vs ratios (2.5–2.6), at least within the reasonable range of crack density (<0.1; Crampin & Leary, 1993). For this modeling, we assume an isotropic host rock with a Vp of 3.6 km/s, Vs of 2.0 km/s, and density of 2.3 g/cm^3. Those values are extracted from Unit 3.

Sustaining the overpressure condition within the fluid reservoir will require a relatively impermeable structure above. Laboratory measurements on terrigenous sediments from deep-sea drilling have shown that the porosities gradually decrease with depth, from ~70% at the sea bottom to ~20% at a burial depth of 1.5 km (Kominz et al., 2011). It has also been reported that porosity changes from 70% to 20% for mudrocks correspond to a 3–4 orders of magnitude decrease in permeability (Neuzil, 1994) . Thus, we speculate that the bottom of Unit 3, with a burial depth of ~2.6–3.9 km, undergoes more severe porosity loss and can impede fluid to permeate shallower layers. This permeability barrier could trap abundant fluid below, leading to the formation of the fluid reservoir.

Considering the shallow subduction depth (~ 10 km), subducted sediment along with the Phillippine Sea plate is likely a fluid source, which can release fluid via mechanical compaction or dehydration (Saffer & Tobin, 2011). The occurrence of slow earthquakes may reflect fluid-rich conditions near the subducting plate interface: lines of evidence require high pore fluid pressure for the genesis of slow earthquakes (Behr & Bürgmann, 2021 and references therein). Since this possible fluid source is spatially separated from the LVZ, permeable structures such as faults or fractures will be required to effectively convey fluids from the subducted sediments to the LVZ, as discussed in the next paragraph. Such permeable structures may not penetrate Unit 3. After reaching the bottom of Unit 3, fluids might diffuse laterally in accordance with permeability anisotropy due to sediment stratification.

The presence of faults in the overriding prism seems natural for this region with the subducted KPR. Analog and numerical experiments have demonstrated that many back-thrusts occur on the leading flank of the seamount (Dominguez et al., 1998; Sun et al., 2020). A recent compilation of seismic reflection surveys in the Hyuga-nada has identified several NNW–SSE trending thrust faults northeast to the array (Figure 9; Headquarters for Earthquake Research Promotion, 2020). At ~2 Ma, before the last change in the convergence direction, the KPR was located east of the present position (Mahony et al., 2011). The subsequent oblique subduction involves right-lateral motion along the trench, potentially inducing the northeast-dipping back-thrust near the array (Figure 10a). Notably, this fault trend is roughly parallel to the sharp offset in the LVZ depth we observed. The sharp offset could imply the presence of a blind back-thrust fault beneath it. Cumulative deformation along the fault might be responsible for the sharp offset. If existing, such a fault will act as a fluid conduit (Figure 10a).

We acknowledge that our dataset poses only weak constraints on the geological process behind the LVZ and thus does not exclude other possibilities. For another hypothesis, the LVZ could represent ascending, overpressured material, such as a mud diapir (e.g., Brown, 1990), about to pierce into Unit 3 (Figure 10b). The head of ascending body would selectively intrude into Unit 3 along a mechanically weakened fabric parallel to the KPR, which leads to the NNW-SSE trending depth offset. Similarly oriented faults nearby the array (Figure 9) support the presence of such a weak fabric. Further investigation in combination with active-source seismic surveys can illuminate the cause of this LVZ but is left for our future work.

This study has identified that the LVZ extends laterally, at least to the array size (~4 km). The Vp gradient profile shown in Figure 1d suggests that the LVZ extends ~60 km laterally beyond the aperture of the OBS array. Moreover, an independent seismic refraction profile in Hyuga-nada has obtained a comparable low-velocity feature within the accretionary prism, ~50–100 km south of the array (Nishizawa et al., 2009), possibly suggesting that similar fluid reservoirs are widely distributed in this region. Pursuing its spatial extent will be important for better understanding the cause of the LVZ and hydrological processes of Hyuga-nada in association with the KPR.

6. Conclusions

In this study, the Vs structure in the Hyuga-nada accretionary prism was constrained using a passive seismic array. The Vs structure exhibits a LVZ beneath stratified sedimentary units (U1–3). Based on the reduced Vs and high Vp/Vs ratio, we conclude that the LVZ reflects a fluid reservoir with high pore fluid pressure sustained by the impermeable layering above. The significant depth offset of the top of the LVZ, extending over ~4 km of the array aperture, possibly suggests the presence of a blind thrust fault or fractures. Such faults generated by the subduction of the KPR may act as fluid pathways and contribute to the reservoir. However, we do not exclude other possibilities: the LVZ may reflect a mud diapir, for example.

The results of this study demonstrate the potential of passive seismic source analyses to acquire a high-resolution structure of Vs, leading to gaining new constraints on fluid processes in the accretionary system. A limitation is its narrow resolvable range laterally, which may hamper interpreting resultant Vs structures conclusively. Joint interpretation with active seismic source surveys will remedy this drawback. Nowadays, a number of seismic survey data have been obtained in subduction zones worldwide. Additional passive seismic experiments like this study will help understand physical properties and hydrological features in the accretionary prism.

Acknowledgments

We thank three anonymous reviewers for their constructive comments. We also thank Ryuta Arai for his valuable discussion, which helped conceptualize this study. This study was supported by JSPS KAKENHI Grant Number 19K14811 and by the Ministry of Education, Culture, Sports, Science and Technology (MEXT) of Japan, under its Earthquake and Volcano Hazards Observation and Research Program.

Data availability

The teleseismic P-waves and ambient noise cross-correlation functions used in this study is available at Zenodo repository (https://doi.org/10.5281/zenodo.7344432). A computer program for the deconvolution of teleseismic waveforms is available at GitHub repository (https://github.com/akuhara/MC3deconv) or Zenodo repository (https://doi.org/10.5281/zenodo.2548974). A computer program for transdimensional inversion is available at GitHub repository (https://github.com/akuhara/SEIS_FILO) or Zenodo repository (https://doi.org/10.5281/zenodo.6330840). The Vp models of Nakanishi et al. (2018) are available upon request through the JAMSTEC Seismic Survey Database (JAMSTEC, 2004).

References

Agius, M. R., Harmon, N., Rychert, C. A., Tharimena, S., & Kendall, J. M. (2018). Sediment Characterization at the Equatorial Mid-Atlantic Ridge From P-to-S Teleseismic Phase Conversions Recorded on the PI-LAB Experiment. *Geophysical Research Letters*, *45*(22), 12,244-12,252. https://doi.org/10.1029/2018GL080565

Akuhara, T., Bostock, M. G., Plourde, A. P., & Shinohara, M. (2019). Beyond Receiver Functions: Green's Function Estimation by Transdimensional Inversion and Its Application to OBS Data. *Journal of Geophysical Research: Solid Earth*, *124*(2), 1944–1961. https://doi.org/10.1029/2018JB016499

Akuhara, T., Tsuji, T., & Tonegawa, T. (2020). Overpressured Underthrust Sediment in the Nankai Trough Forearc Inferred From Transdimensional Inversion of High-Frequency Teleseismic Waveforms. *Geophysical Research Letters*, *47*(15). https://doi.org/10.1029/2020GL088280

Arnulf, A. F., Biemiller, J., Lavier, L., Wallace, L. M., Bassett, D., Henrys, S., et al. (2021). Physical conditions and frictional properties in the source region of a slow-slip event. *Nature Geoscience*, *14*(5), 334–340. https://doi.org/10.1038/s41561-021-00741-0

Baba, S., Takemura, S., Obara, K., & Noda, A. (2020). Slow Earthquakes Illuminating Interplate Coupling Heterogeneities in Subduction Zones. *Geophysical Research*

Letters, *47*(14), 4–5. https://doi.org/10.1029/2020GL088089

Behr, W. M., & Bürgmann, R. (2021). *What's down there? The structures, materials and environment of deep-seated slow slip and tremor*. *Philosophical Transactions of the Royal Society A: Mathematical, Physical and Engineering Sciences* (Vol. 379). https://doi.org/10.1098/rsta.2020.0218

Bensen, G. D., Ritzwoller, M. H., Barmin, M. P., Levshin, A. L., Lin, F., Moschetti, M. P., et al. (2007). Processing seismic ambient noise data to obtain reliable broad-band surface wave dispersion measurements. *Geophysical Journal International*, *169*(3), 1239–1260. https://doi.org/10.1111/j.1365-246X.2007.03374.x

Bodin, T., Sambridge, M., Tkalćić, H., Arroucau, P., Gallagher, K., & Rawlinson, N. (2012). Transdimensional inversion of receiver functions and surface wave dispersion. *Journal of Geophysical Research: Solid Earth*, *117*(2), 1–24. https://doi.org/10.1029/2011JB008560

Brocher, T. M. (2005). Empirical relations between elastic wavespeeds and density in the Earth's crust. *Bulletin of the Seismological Society of America*, *95*(6), 2081–2092. https://doi.org/10.1785/0120050077

Brown, K. M. (1990). The nature and hydrogeologic significance of mud diapirs and diatremes for accretionary systems. *Journal of Geophysical Research*, *95*(B6), 8969. https://doi.org/10.1029/JB095iB06p08969

Chesley, C., Naif, S., Key, K., & Bassett, D. (2021). Fluid-rich subducting topography generates anomalous forearc porosity. *Nature*, *595*(7866), 255–260. https://doi.org/10.1038/s41586-021-03619-8

Crampin, S., & Leary, P. C. (1993). Limits to crack density: The state of fractures in crustal rocks. In *SEG Technical Program Expanded Abstracts 1993* (pp. 758–761). Society of Exploration Geophysicists. https://doi.org/10.1190/1.1822609

Van Dinther, Y., Gerya, T. V., Dalguer, L. A., Mai, P. M., Morra, G., & Giardini, D. (2013). The seismic cycle at subduction thrusts: Insights from seismo-thermo-mechanical models. *Journal of Geophysical Research: Solid Earth*, *118*(12), 6183–6202. https://doi.org/10.1002/2013JB010380

Dominguez, S., Lallemand, S. ., Malavieille, J., & von Huene, R. (1998). Upper plate deformation associated with seamount subduction. *Tectonophysics*, *293*(3–4), 207–224. https://doi.org/10.1016/S0040-1951(98)00086-9

Doran, A. K., & Laske, G. (2019). Seismic Structure of Marine Sediments and Upper Oceanic Crust Surrounding Hawaii. *Journal of Geophysical Research: Solid Earth*, *124*(2), 2038–2056. https://doi.org/10.1029/2018JB016548

Dosso, S. E., Dettmer, J., Steininger, G., & Holland, C. W. (2014). Efficient trans-dimensional Bayesian inversion for geoacoustic profile estimation. *Inverse Problems*, *30*(11), 114018. https://doi.org/10.1088/0266-5611/30/11/114018

Dvorkin, J., Mavko, G., & Nur, A. (1999). Overpressure detection from compressional- and shear-wave data. *Geophysical Research Letters*. https://doi.org/10.1029/1999GL008382

Geyer, C. J., & Thompson, E. A. (1995). Annealing Markov Chain Monte Carlo with Appplications to Ancestral Inference. *J. Am. Stat. Assoc.*, *90*(431), 909–920. https://doi.org/10.1080/01621459.1995.10476590

Gouédard, P., Cornou, C., & Roux, P. (2008). Phase-velocity dispersion curves and small-scale geophysics using noise correlation slantstack technique. *Geophysical Journal International*, *172*(3), 971–981. https://doi.org/10.1111/j.1365-246X.2007.03654.x

Green, P. J. (1995). Reversible jump Markov chain monte carlo computation and Bayesian model determination. *Biometrika*, *82*(4), 711–732. https://doi.org/10.1093/biomet/82.4.711

Hamilton, E. L. (1979). V_p / V_s and Poisson's ratios in marine sediments and rocks. *The Journal of the Acoustical Society of America*, *66*(4), 1093–1101. https://doi.org/10.1121/1.383344

Headquarters for Earthquake Research Promotion (2020). Comprehensive assessment of fault information in marine areas (in Japanese). Retrieved from https://www.jishin.go.jp/main/chousakenkyuu/kaiiki/r01/R01kaiiki_3_2.pdf

Hudson, J. A. (1981). Wave speeds and attenuation of elastic waves in material containing cracks. *Geophysical Journal of the Royal Astronomical Society*, *64*(1), 133–150. https://doi.org/10.1111/j.1365-246X.1981.tb02662.x

Itoh, Y., Takemura, K., & Kamata, H. (1998). History of basin formation and tectonic evolution at the termination of a large transcurrent fault system: deformation mode of central Kyushu, Japana. *Tectonophysics*, *284*(1–2), 135–150. https://doi.org/10.1016/S0040-1951(97)00167-4

JAMSTEC. (2004). JAMSTEC Seismic Survey Database. https://doi.org/10.17596/0002069

Kominz, M. A., Patterson, K., & Odette, D. (2011). Lithology dependence of porosity in slope and deep marine sediments. *Journal of Sedimentary Research*, *81*(10), 730–742. https://doi.org/10.2110/jsr.2011.60

Mahony, S. H., Wallace, L. M., Miyoshi, M., Villamor, P., Sparks, R. J., & Hasenaka, T. (2011). Volcano-tectonic interactions during rapid plate-boundary evolution in the Kyushu region, SW Japan. *Bulletin of the Geological Society of America*, *123*(11–

12), 2201–2223. https://doi.org/10.1130/B30408.1

Mosher, S. G., Eilon, Z., Janiszewski, H., & Audet, P. (2021). Probabilistic inversion of seafloor compliance for oceanic crustal shear velocity structure using mixture density neural networks. *Geophysical Journal International*, *227*(3), 1879–1892. https://doi.org/10.1093/gji/ggab315

Nakanishi, A., Takahashi, N., Yamamoto, Y., Takahashi, T., Ozgur Citak, S., Nakamura, T., et al. (2018). Three-dimensional plate geometry and P-wave velocity models of the subduction zone in SW Japan: Implications for seismogenesis. In T. Byrne, I. Underwood, Michael B., D. Fisher, L. McNeill, D. Saffer, K. Ujiie, & A. Yamaguchi (Eds.), *Geology and Tectonics of Subduction Zones: A Tribute to Gaku Kimura*. Geological Society of America. https://doi.org/10.1130/2018.2534(04)

Neuzil, C. E. (1994). How permeable are clays and shales? *Water Resources Research*, *30*(2), 145–150. https://doi.org/10.1029/93WR02930

Nishizawa, A., Kaneda, K., & Oikawa, M. (2009). Seismic structure of the northern end of the Ryukyu Trench subduction zone, southeast of Kyushu, Japan. *Earth, Planets and Space*, *61*(8), e37–e40. https://doi.org/10.1186/bf03352942

Park, J. O., Hori, T., & Kaneda, Y. (2009). Seismotectonic implications of the Kyushu-Palau ridge subducting beneath the westernmost Nankai forearc. *Earth, Planets and Space*, *61*(8), 1013–1018. https://doi.org/10.1186/BF03352951

Prasad, M. (2002). Acoustic measurements in unconsolidated sands at low effective pressure and overpressure detection. *Geophysics*, *67*(2), 405–412. https://doi.org/10.1190/1.1468600

Saffer, D. M., & Tobin, H. J. (2011). Hydrogeology and Mechanics of Subduction Zone Forearcs: Fluid Flow and Pore Pressure. *Annual Review of Earth and Planetary Sciences*, *39*(1), 157–186. https://doi.org/10.1146/annurev-earth-040610-133408

Saffer, D. M., & Wallace, L. M. (2015). The frictional, hydrologic, metamorphic and thermal habitat of shallow slow earthquakes. *Nature Geoscience*, *8*(8), 594–600. https://doi.org/10.1038/ngeo2490

Sahling, H., Masson, D. G., Ranero, C. R., Hühnerbach, V., Weinrebe, W., Klaucke, I., et al. (2008). Fluid seepage at the continental margin offshore Costa Rica and southern Nicaragua. *Geochemistry, Geophysics, Geosystems*, *9*(5). https://doi.org/10.1029/2008GC001978

Sambridge, M. (2014). A Parallel Tempering algorithm for probabilistic sampling and multimodal optimization. *Geophysical Journal International*, *196*(1), 357–374. https://doi.org/10.1093/gji/ggt342

Sawaki, Y., Yamashita, Y., Ohyanagi, S., Garcia, E. S. M., Ito, A., Sugioka, H., et al.

(2022). Seafloor depth controls seismograph orientation uncertainty. *Geophysical Journal International*. https://doi.org/10.1093/gji/ggac397
Stachnik, J. C., Sheehan, A. F., Zietlow, D. W., Yang, Z., Collins, J., & Ferris, A. (2012). Determination of New Zealand Ocean Bottom Seismometer Orientation via Rayleigh-Wave Polarization. *Seismological Research Letters*, *83*(4), 704–713. https://doi.org/10.1785/0220110128
Sun, T., Saffer, D., & Ellis, S. (2020). Mechanical and hydrological effects of seamount subduction on megathrust stress and slip. *Nature Geoscience*, *13*(3), 249–255. https://doi.org/10.1038/s41561-020-0542-0
Tonegawa, T., Araki, E., Kimura, T., Nakamura, T., Nakano, M., & Suzuki, K. (2017). Sporadic low-velocity volumes spatially correlate with shallow very low frequency earthquake clusters. *Nature Communications*, *8*(1), 2048. https://doi.org/10.1038/s41467-017-02276-8
Tonegawa, T., Yamashita, Y., Takahashi, T., Shinohara, M., Ishihara, Y., Kodaira, S., & Kaneda, Y. (2020). Spatial relationship between shallow very low frequency earthquakes and the subducted Kyushu-Palau Ridge in the Hyuga-nada region of the Nankai subduction zone. *Geophysical Journal International*, *222*(3), 1542–1554. https://doi.org/10.1093/gji/ggaa264
Tsuji, T., Dvorkin, J., Mavko, G., Nakata, N., Matsuoka, T., Nakanishi, A., et al. (2011). V P / V S ratio and shear-wave splitting in the Nankai Trough seismogenic zone: Insights into effective stress, pore pressure, and sediment consolidation. *Geophysics*, *76*(3), WA71–WA82. https://doi.org/10.1190/1.3560018
Wang, K., & Hu, Y. (2006). Accretionary prisms in subduction earthquake cycles : The theory of dynamic Coulomb wedge, *111*(March), 1–16. https://doi.org/10.1029/2005JB004094
Yamagishi, Y., Nakanishi, A., Miura, S., Kodaira, S., & Sakaguchi, H. (2018). Development of a database and visualization system integrating various models of seismic velocity structure and subducting plate geometry around Japan. *Progress in Earth and Planetary Science*, *5*(1). https://doi.org/10.1186/s40645-018-0207-4
Yamamoto, Y., Obana, K., Takahashi, T., Nakanishi, A., Kodaira, S., & Kaneda, Y. (2013). Imaging of the subducted kyushu-palau ridge in the hyuga-nada region, western nankai trough subduction zone. *Tectonophysics*, *589*, 90–102. https://doi.org/10.1016/j.tecto.2012.12.028
Yamashita, Y., Yakiwara, H., Asano, Y., Shimizu, H., Uchida, K., Hirano, S., et al. (2015). Migrating tremor off southern Kyushu as evidence for slow slip of a shallow subduction interface. *Science*, *348*(6235), 676–679.

https://doi.org/10.1126/science.aaa4242

Yamashita, Y., Shinohara, M., & Yamada, T. (2021). Shallow tectonic tremor activities in Hyuga-nada, Nankai subduction zone, based on long-term broadband ocean bottom seismic observations. *Earth, Planets and Space*, *73*(1). https://doi.org/10.1186/s40623-021-01533-x

Yamaya, L., Mochizuki, K., Akuhara, T., & Nishida, K. (2021). Sedimentary Structure Derived From Multi-Mode Ambient Noise Tomography With Dense OBS Network at the Japan Trench. *Journal of Geophysical Research: Solid Earth*, *126*(6), 1–20. https://doi.org/10.1029/2021JB021789

Yamazaki, T., & Okamura, Y. (1989). Subducting seamounts and deformation of overriding forearc wedges around Japan. *Tectonophysics*, *160*(1–4), 207–229. https://doi.org/10.1016/0040-1951(89)90392-2

Zhang, X., Hansteen, F., Curtis, A., & de Ridder, S. (2020). 1-D, 2-D, and 3-D Monte Carlo Ambient Noise Tomography Using a Dense Passive Seismic Array Installed on the North Sea Seabed. *Journal of Geophysical Research: Solid Earth*, *125*(2), 1–32. https://doi.org/10.1029/2019JB018552

Zhu, L., Kanamori, H. (2000). Moho depth variation in southern California. *Journal of Geophysical Research*, *105*, 2969–2980. https://doi.org/10.1029/1999JB900322

Figure legends

Figure 1. Tectonic setting of the study area and array configuration. (a) The orange star denotes the location of an array of ocean-bottom seismometers. The red line represents the cross-section shown in (c) and (d). Yellow dots represent the epicenters of the tectonic tremors (Yamashita et al., 2015, 2021). The pink line denotes the subducted Kyushu-Palau Ridge (Yamamoto et al., 2013). (b) Array configuration. The gray contour indicates the water depth, with an interval of 10 m. (c) P-wave velocity model obtained from a refraction survey (Nakanishi et al., 2018). The yellow inverse triangles represent the locations of ocean-bottom seismometers. The subducting plate interface is denoted by the black line, which is defined by the velocity gradient profile of (d). (d) The same as (c), but vertical velocity gradients are shown. PHP: Philippine Sea Plate.

Figure 2. Ambient noise cross-correlation functions filtered from 0.2 to 0.4 Hz. Cross-correlation functions from all pairs of stations are displayed against their inter-station distances. The green line corresponds to a propagation speed of 0.5 km/s.

Figure 3. Frequency-wavenumber diagram calculated from ambient noise cross-correlations. The white dashed line indicates the resolution limit (Gouédard et al., 2008). Note that the power spectrum is normalized at each frequency.

Figure 4. Green’s functions estimated for teleseismic P-waves: (a) radial and (b) vertical components. The stations are sorted by their locations from WSW to ENE.

Figure 5. Joint inversion results for station HDA06. (a–c) Posterior probability of the (a) number of layers, (b) standard deviation of the noise in phase velocity data, and (c) standard deviation of the noise in Green’s function data. (d–e) Input data (blue circlesor curve), distribution of model predictions (yellow–red heatmap), and the maximum a posteriori (MAP) predictions (purple curves) for the (d) dispersion curve and (e) Green’s function. (f) Posterior marginal probability of the S-wave velocity as a function of depth. The yellow–red heatmap indicates the probability; low probabilities (<0.01) are transparently masked. The black line represents the reference velocity model. The green line indicates the mode estimation (i.e., the maximum probability at each depth). The purple line is the MAP estimation. Background colors discriminate the different lithologies identified in this study.

Figure 6. Joint inversion results for all stations. Each panel shows the posterior marginal probabilities of the S-wave velocity as a function of depth obtained for different stations. The notations are the same as those in Figure 5f.

Figure 7. Vp/Vs estimations for all stations. The probability distribution of Vp/Vs is calculated from Vs profile sampled by inversion and the reference Vp model, where the former Vs profile is smoothed over depths with a running window of 1.5 km. Notations are the same as Figure 6.

Figure 8. Lithology depths. (a) The depth of the top of the low-velocity zone (LVZ). The station HDA01, whose velocity structure does not show an evident LVZ, is filled in black. (b) Lithology top depths along the profile X–Y shown in (a). The square, triangle, circle, and inverted triangle symbols denote the sedimentary units 2 (U2), 3 (U3), LVZ, and deeper lithology, respectively. The black line represents the average seafloor depth across the array. Error bars are 68% confidence intervals of the lithology depth. For HDA01, the depth of LVZ top is not shown because of its absence in the results. (c) Teleseismic Green's function at each station. The blue wiggles represent the observed stacked GFs. The dotted purple lines are the predictions from the maximum a posteriori estimations. The yellow–red heatmap represents the frequency distribution of the model predictions. The green vertical bars indicate 68% confidence intervals of the arrival time of Ps converted phases from the top of the LVZ. Again, the arrival time of HDA01 is not shown due to the absence of the LVZ.

Figure 9. Fault traces from a compilation of seismic reflection surveys (Headquarters for Earthquake Research Promotion, 2020). The sky-blue, green, and purple lines denote thrust, strike-slip, and normal faults, respectively. The orange star denotes the location of an array of ocean-bottom seismometers. The pink line denotes the subducted Kyushu-Palau Ridge (Yamamoto et al., 2013).

Figure 10. Schematic illustration of possible causes of the low-velocity zone (LVZ) and its depth offset. (a) A scenario by a blind fault. A blind fault induced by the subducted Kyushu–Palau Ridge may act as fluid conduits to form the fluid reservoir. (b) Alternative scenario by mud diapir. An overpressured mud diapir pierces into Unit 3.

Figure 1.

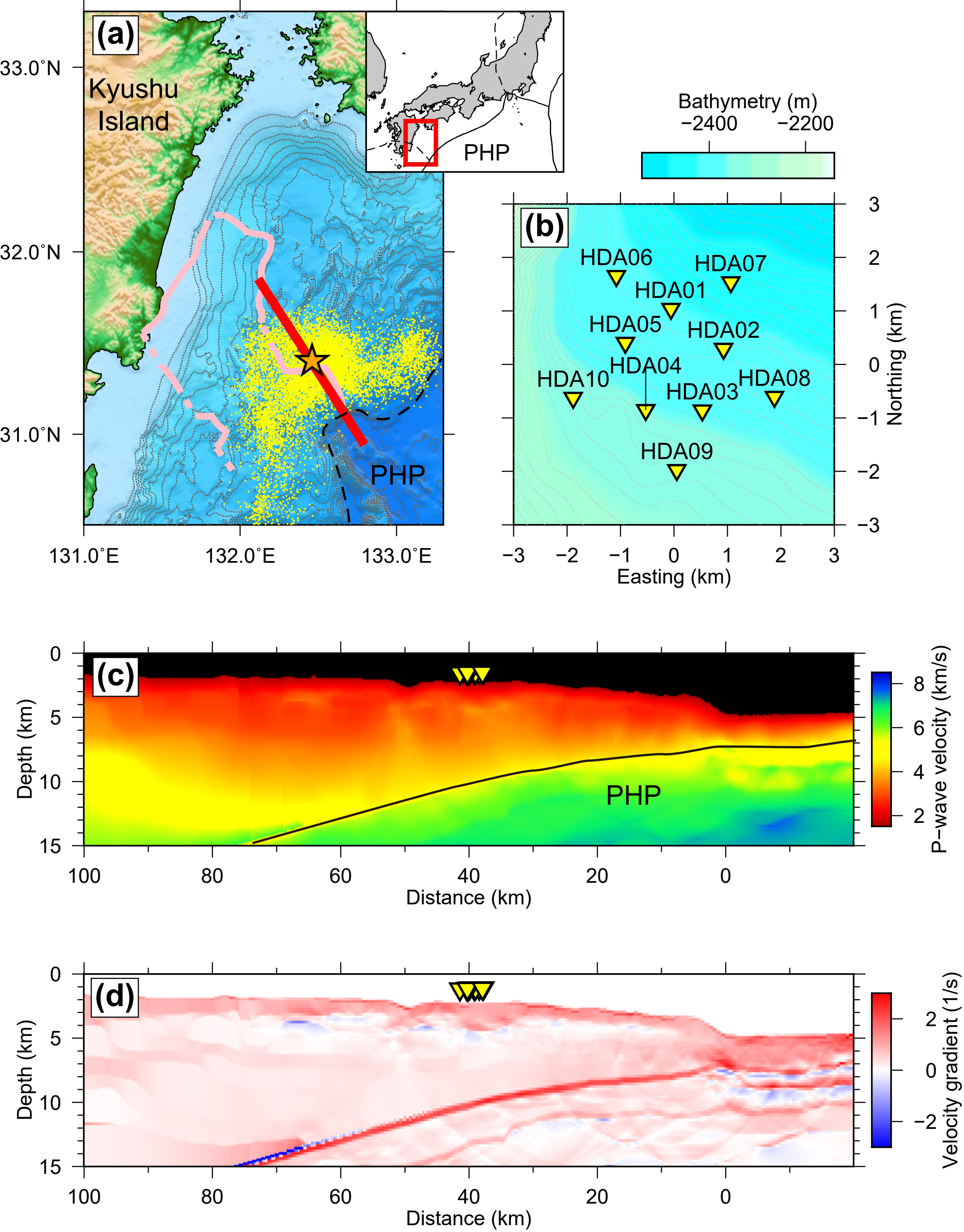

(a)
33.0˚N
32.0˚N
31.0˚N
131.0˚E
132.0˚E
133.0˚E
Kyushu Island
PHP
PHP
Bathymetry (m)
−2400
−2200
(b)
HDA06
HDA07
HDA01
HDA05
HDA02
HDA04
HDA10
HDA08
HDA03
HDA09
Easting (km)
Northing (km)
(c)
Depth (km)
Distance (km)
PHP
P−wave velocity (km/s)
(d)
Depth (km)
Distance (km)
Velocity gradient (1/s)

Figure 2.

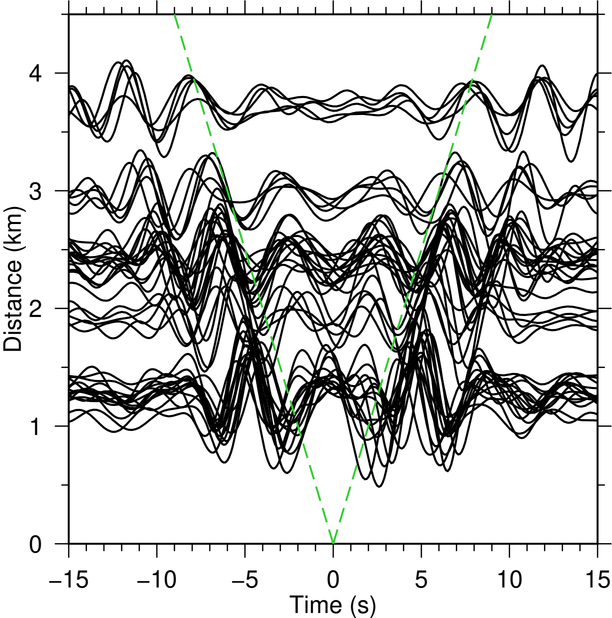

Distance (km)
0
1
2
3
4
Time (s)
–15
–10
–5
0
5
10
15

Figure 3.

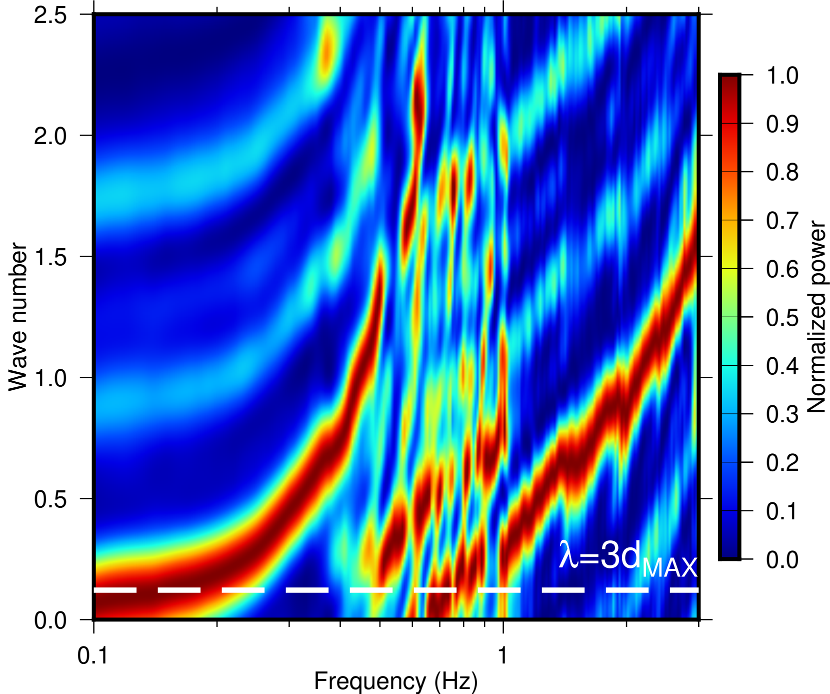

2.5
2.0
1.5
1.0
0.5
0.0
Wave number
0.1
1
Frequency (Hz)
λ=3d
MAX
1.0
0.9
0.8
0.7
0.6
0.5
0.4
0.3
0.2
0.1
0.0
Normalized power

Figure 4.

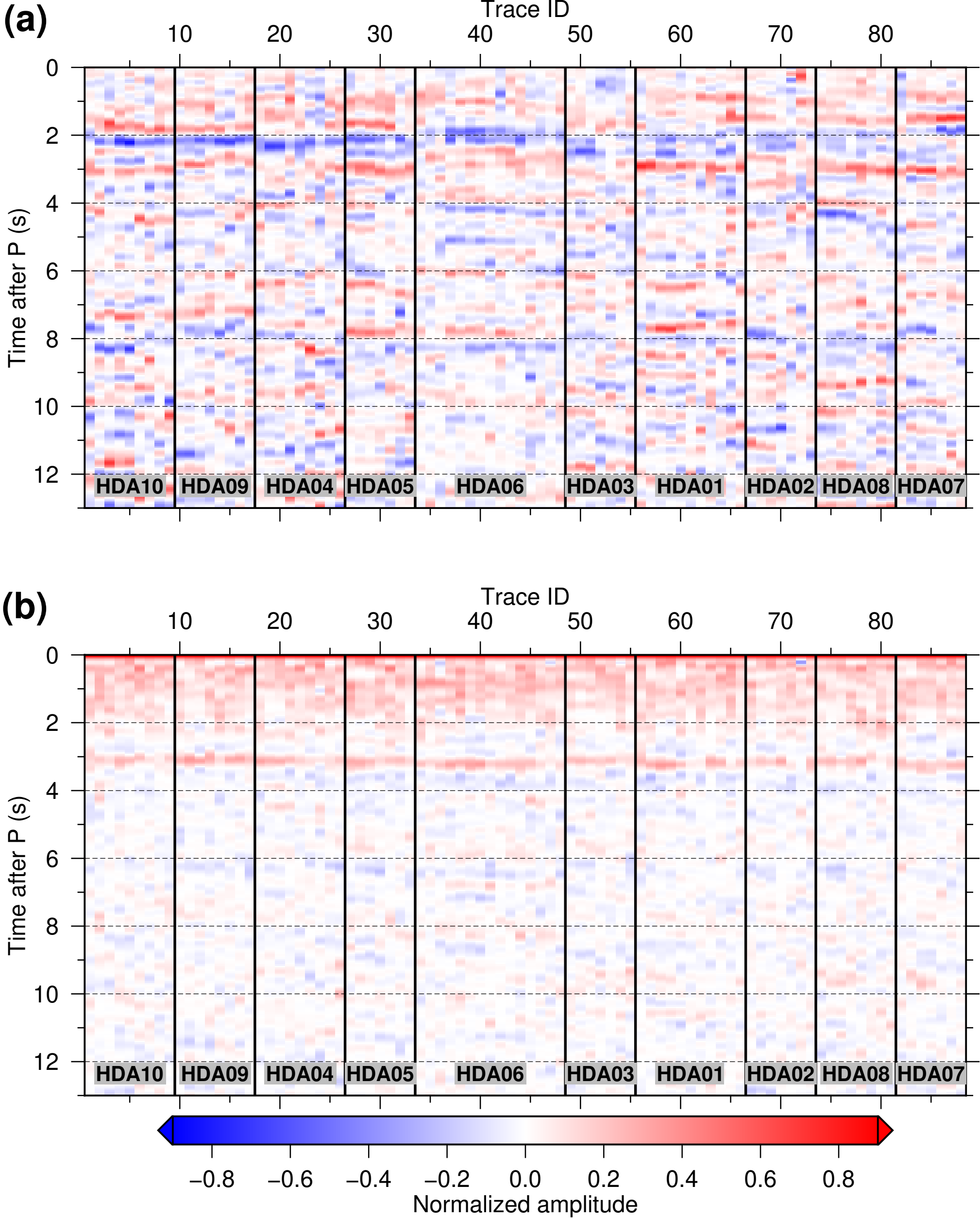

(a)
Trace ID
10 20 30 40 50 60 70 80
Time after P (s)
0 2 4 6 8 10 12
HDA10 HDA09 HDA04 HDA05 HDA06 HDA03 HDA01 HDA02 HDA08 HDA07
(b)
Trace ID
10 20 30 40 50 60 70 80
Time after P (s)
0 2 4 6 8 10 12
HDA10 HDA09 HDA04 HDA05 HDA06 HDA03 HDA01 HDA02 HDA08 HDA07
−0.8 −0.6 −0.4 −0.2 0.0 0.2 0.4 0.6 0.8
Normalized amplitude

Figure 5.

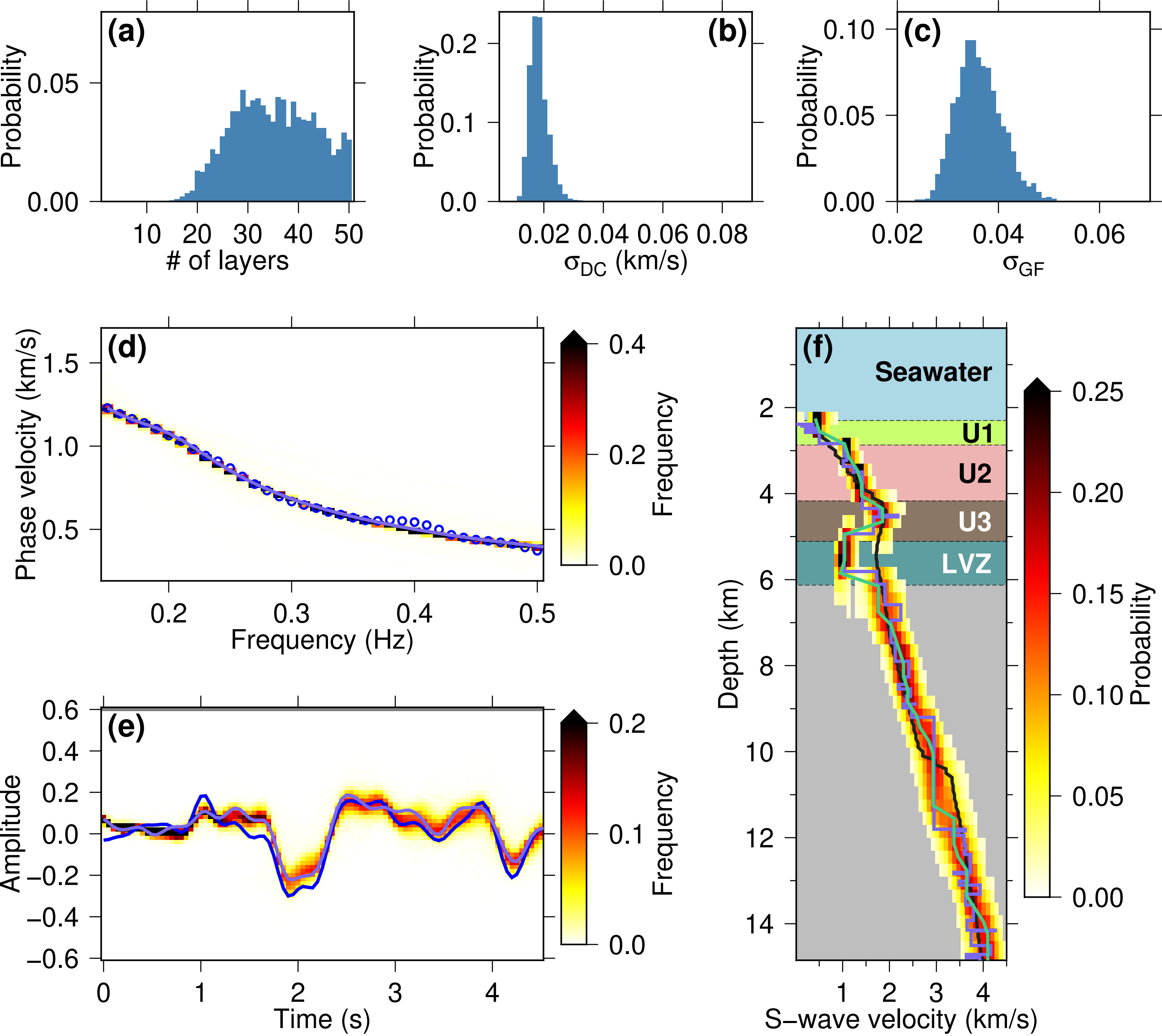

(a)
Probability
# of layers
(b)
σ_{DC} (km/s)
(c)
σ_{GF}
(d)
Phase velocity (km/s)
Frequency (Hz)
Frequency
(e)
Amplitude
Time (s)
Frequency
(f)
Seawater
U1
U2
U3
LVZ
Depth (km)
S−wave velocity (km/s)
Probability

Figure 6.

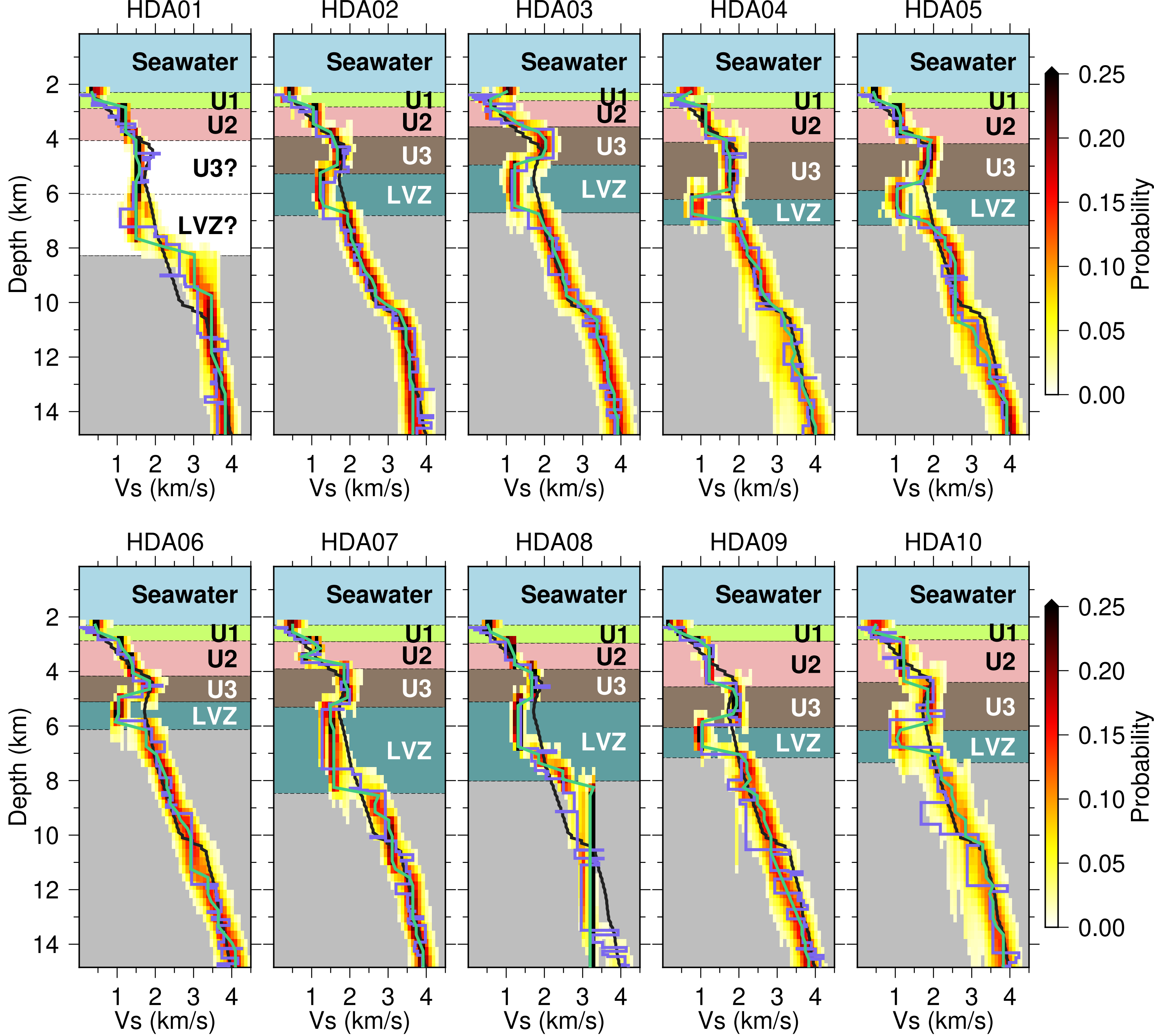
HDA01
HDA02
HDA03
HDA04
HDA05
HDA06
HDA07
HDA08
HDA09
HDA10
Seawater
U1
U2
U3
U3?
LVZ
LVZ?
Depth (km)
Vs (km/s)
Probability
0.00
0.05
0.10
0.15
0.20
0.25

Figure 7.

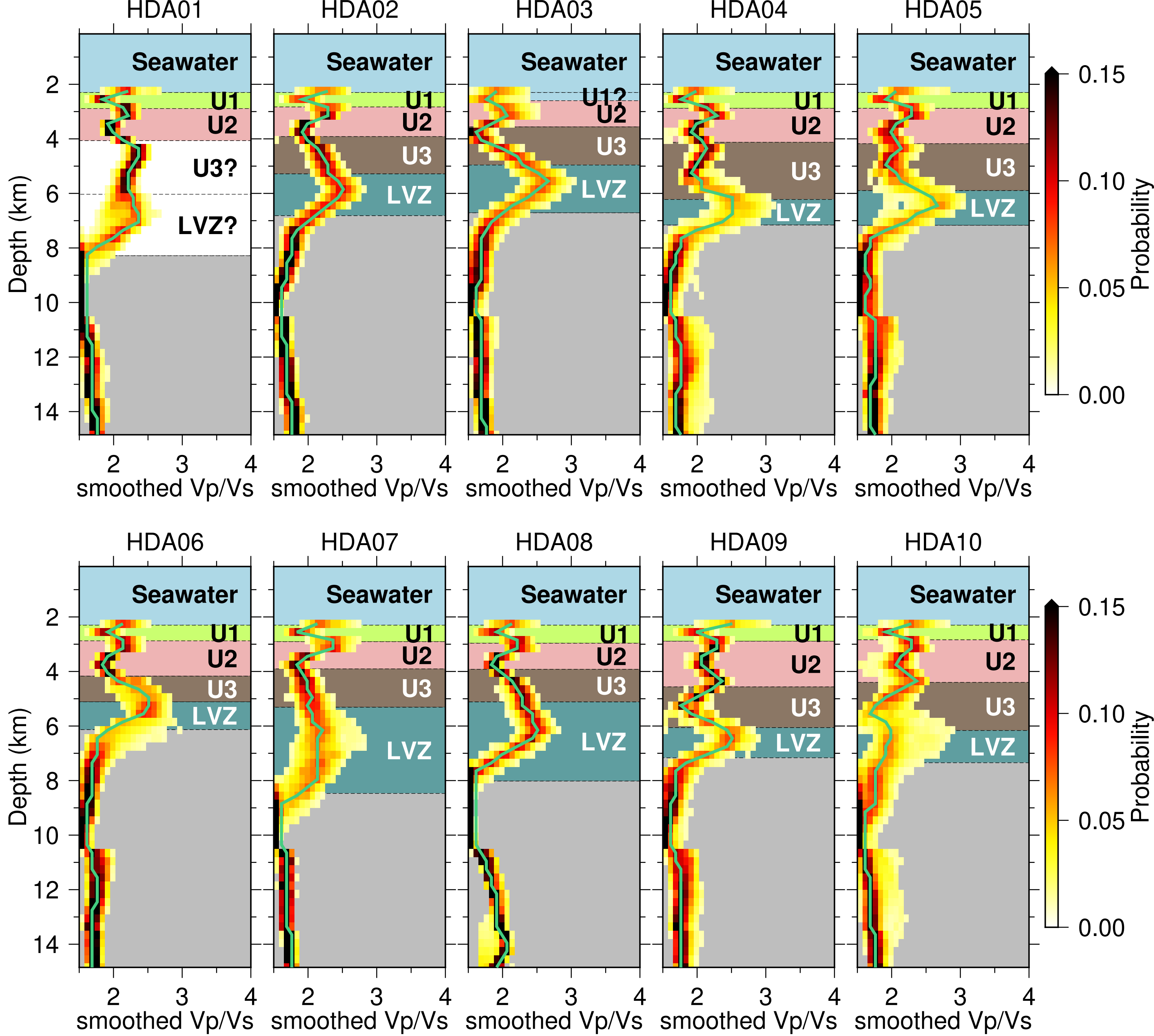
HDA01
HDA02
HDA03
HDA04
HDA05
HDA06
HDA07
HDA08
HDA09
HDA10
Seawater
U1
U1?
U2
U3
U3?
LVZ
LVZ?
Depth (km)
smoothed Vp/Vs
Probability
0.15
0.10
0.05
0.00

Figure 8.

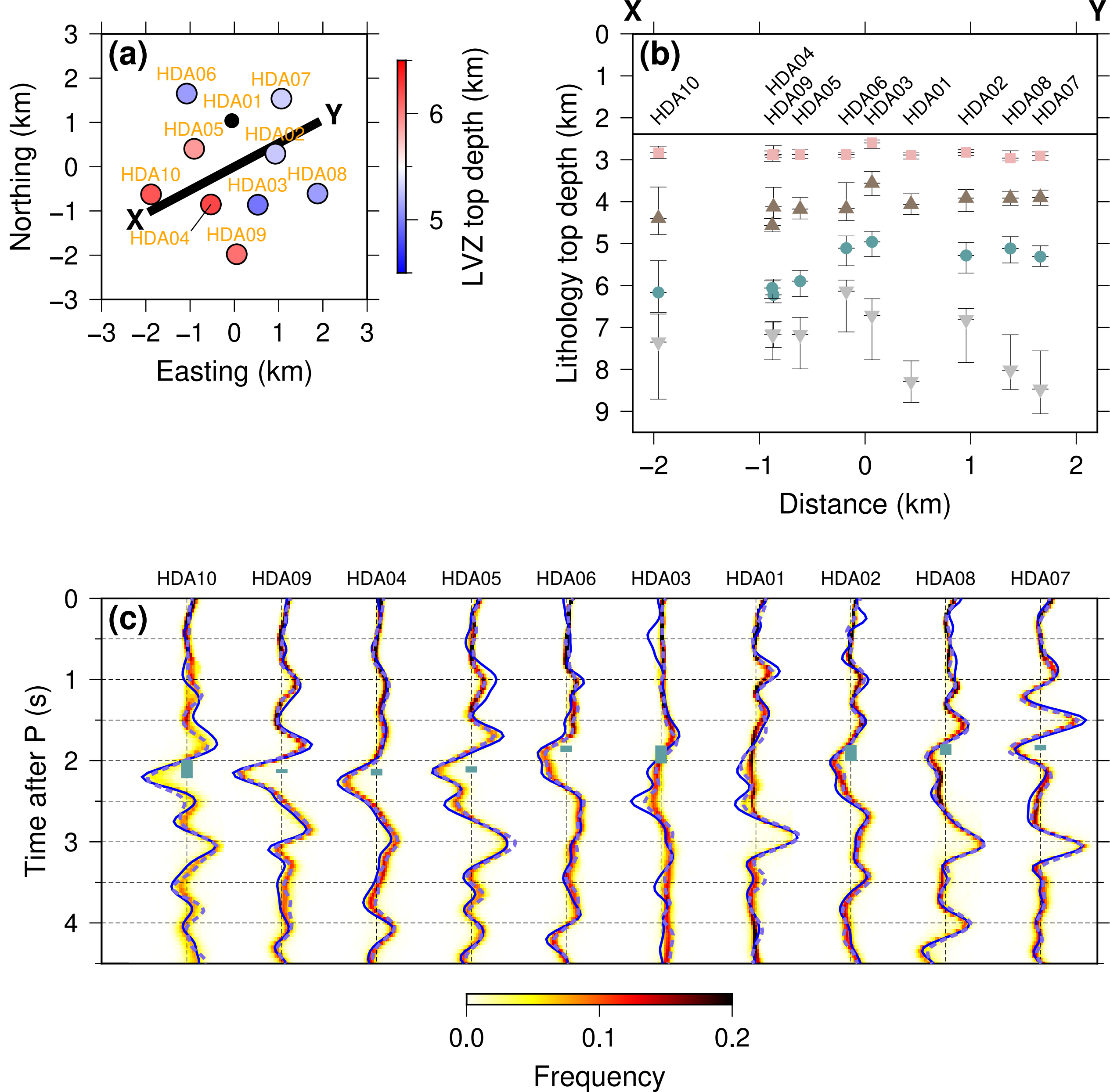

(a)
HDA06
HDA07
HDA01
Y
HDA05
HDA02
HDA10
HDA08
HDA03
X
HDA04
HDA09
Northing (km)
Easting (km)
LVZ top depth (km)
(b)
X
Y
HDA10
HDA04
HDA09
HDA05
HDA06
HDA03
HDA01
HDA02
HDA08
HDA07
Lithology top depth (km)
Distance (km)
(c)
HDA10
HDA09
HDA04
HDA05
HDA06
HDA03
HDA01
HDA02
HDA08
HDA07
Time after P (s)
Frequency

Figure 9.

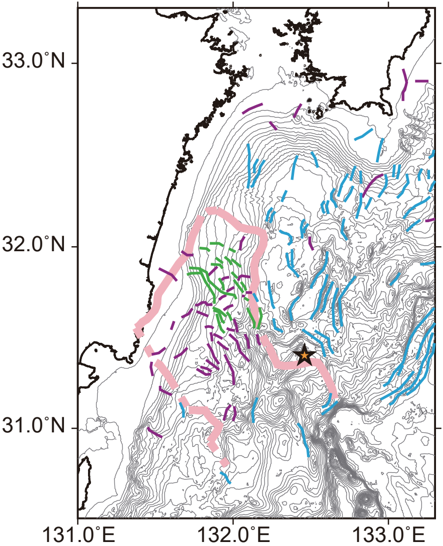
33.0˚N
32.0˚N
31.0˚N
131.0˚E
132.0˚E
133.0˚E

Figure 10.

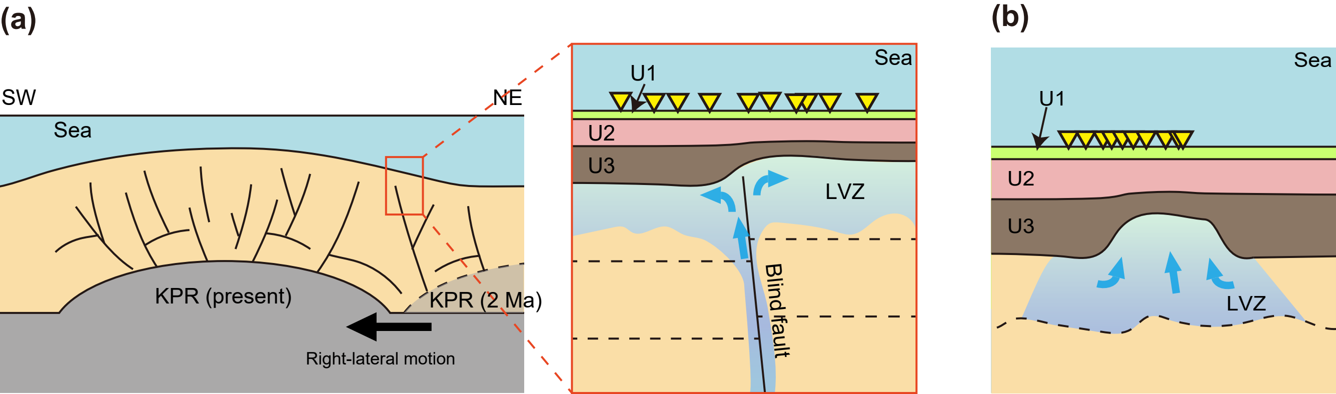
(a)
SW
NE
Sea
KPR (present)
KPR (2 Ma)
Right-lateral motion
Sea
U1
U2
U3
LVZ
Blind fault
(b)
Sea
U1
U2
U3
LVZ